



ORIGINAL RESEARCH ARTICLE

Preparation and Anticorrosion Performance of Double-Layer Epoxy Resin Coatings on Bonded NdFeB Magnets

Youwen Yang, Yingzhong Sun, Lei Yang, Lushui Su, Mengke Jia, Yufan Chen, Xiaogang Fang, and Jiguang Liu

Submitted: 24 July 2023 / Revised: 11 October 2023 / Accepted: 4 November 2023

Double-layer epoxy resin coatings (C-EP) were prepared on the surface of ring-shaped bonded NdFeB (RSM) by cathodic electrophoretic deposition and air spraying for the first time. The surface morphology and chemical composition of C-EP were characterized by scanning electron microscopy (SEM), energy dispersive spectroscopy (EDS) and atomic force microscopy (AFM). The digital microhardness tester was utilized to measure the microhardness of C-EP/RSM, which was found to be 33.623 HV, slightly higher than that of electrophoretic EP/RSM (E-EP/RSM). The corrosion-resistant performance of C-EP/RSM was evaluated through polarization curves and neutral salt spray (NSS) tests, with a discussion on the corrosion mechanism. The results indicate that the epoxy resin particles effectively penetrate into the pores of NdFeB matrix, exhibiting excellent sealing properties. The structure of C-EP is stable, and these two layers together contribute to better anti-corrosion performance. Compared to bare RSM (B-RSM) and E-EP/RSM, the corrosion current density is reduced by approximately one order of magnitude in C-EP/RSM. And, the NSS time of C-EP/RSM reaches 216 h, which is 1.5 times higher than that of E-EP/RSM, indicating superior corrosion resistance. Furthermore, C-EP has little effect on the magnetic properties of RSM.

Keywords air spraying, bonded NdFeB, cathodic electrophoresis deposition, corrosion resistance, double-layer epoxy resin coatings

1. Introduction

Bonded NdFeB magnets are highly valued for their ability to be fabricated into intricate shapes at a relatively low cost, while maintaining their magnetic properties (Ref 1). Consequently, they have become widely utilized in various industries such as new energy vehicles, computers, wind turbines, magnetically levitated transportation systems and aerospace (Ref 2, 3). However, due to inherent structural limitations, bonded NdFeB magnets obtained through molding (Ref 4), injection (Ref 5), extrusion (Ref 6) or calendaring (Ref 7) inevitably suffer from defects such as poor densification and loose porosity. Additionally, the large potential difference between the multiphase

organization of bonded NdFeB magnets leads to a high corrosion tendency of the Nd-rich and B-rich phases distributed between the grains of the main phase (Ref 8). As such, bonded NdFeB magnets exhibit extremely poor resistance to corrosion, making research into their corrosion protection technology particularly crucial. The coating protection method is for the corrosion of NdFeB brought about by the corrosive factors in the external environment, the essence of which is to isolate NdFeB from the external corrosive medium, thus inhibiting the corrosion failure of NdFeB. According to the different composition of coating materials, the coating can be divided into categories such as metal coatings, organic coating and composite coating. While metal coatings offer high strength and hardness, their corrosion resistance is insufficient, and they may reduce the magnetic properties of NdFeB magnets (Ref 9). Organic coatings are primarily composed of organic compounds or polymers. Compared to metal coatings, organic coatings offer superior protection in certain corrosive environments and have less influence on the magnetic properties of magnets. EP, one of the most commonly used resins for preparing organic coatings, boasts excellent chemical stability and substrate adhesion abilities. It is widely utilized in various industrial practices such as coatings, electronic materials, and enclosure materials (Ref 10, 11). However, pure EP coatings still have limitations such as low strength and brittleness that restrict their application in complex environments (Ref 12, 13).

As the application fields of NdFeB continue to expand, the demand for its corrosion resistance becomes increasingly stringent. A single coating is insufficient to meet anti-corrosion requirements. Therefore, combining multiple protection methods has become crucial in further expanding the application areas of NdFeB. To enhance the corrosion resistance of NdFeB,

Youwen Yang, Xiaogang Fang, and Jiguang Liu, School of Materials Science and Engineering, Hefei University of Technology, Hefei 230009 Anhui Province, People's Republic of China; and Engineering Research Center of High-Performance Copper Alloy Material and Forming, Ministry of Education, Hefei University of Technology, Hefei 230009 Anhui Province, People's Republic of China; **Yingzhong Sun, Lei Yang, Lushui Su, and Mengke Jia**, School of Materials Science and Engineering, Hefei University of Technology, Hefei 230009 Anhui Province, People's Republic of China; and **Yufan Chen**, Magnequench Magnetic Materials (Chuzhou) Co., Ltd, Chuzhou 239000, People's Republic of China. Contact e-mail: hfutyw@hfut.edu.cn.

research on metal-organic composite coatings have gained increasing attention in recent years. Liu et al. (Ref 14) utilized electrodeposition and sol-gel techniques to fabricate a Zn/silane composite coating on the surface of NdFeB magnets, which demonstrated superior corrosion resistance compared to pure Zn coating due to the hindering effect of the silane sealing layer. Furthermore, double organic coatings are another type of method with good protection. A double-layer coating consisting of a polyaniline primer and a polytetrafluoroethylene surface-coated epoxy was successfully prepared to provide enhanced corrosion protection for the metal substrate. The impedance modulus of 40 wt.% polyaniline composite coating is four orders of magnitude higher than that of the pure epoxy resin composite coating (Ref 15). This suggests that double-layer coatings exhibit superior corrosion resistance compared to single-layer coating, thereby rendering the development and application of double-layer EP coatings significant. However, the incorporation of excessive amounts of modifiers into EP may pose challenges in terms of composition control and entail high process requirements for mass production, necessitating a simple process approach.

In the previous study, our team used two different processes of electrophoretic deposition and air spraying to prepare EP coating on the surface of bonded NdFeB magnets (Ref 16). Due to the fact that the sprayed EP coating is composed of large molecular groups and electrophoresis is the process of EP cation deposition, the coating pores formed by the electrophoresis process are small, so the corrosion resistance of the EP coating prepared by electrophoresis is better than that of the EP coating prepared by air spraying. To further improve the corrosion resistance of EP coating, the thickness of EP coating can be increased by increasing the electrophoretic voltage. However, when the electrophoretic voltage is excessively increased to increase the thickness of EP coating, the larger suspension point generated by the electrophoretic hanger directly affects the surface smoothness and uniformity of EP coating. At the same time, the use of a single process method to prepare higher thickness of EP coating requires more stringent

conditions and leads to energy and material wastage. Therefore, different processes can be combined to increase the EP coating thickness. According to the literature, there is no report on the preparation of EP coatings by combining electrophoretic deposition and air spraying with each other on the surface of bonded NdFeB magnets. Meanwhile, the use of the same resin in two different processes allows the two layers to bond with each other and the coating structure to become more stable, further improving the corrosion resistance of the surface coating. In this study, C-EP were firstly prepared on the surface of RSM by cathodic electrophoretic deposition and air spraying. The adhesion, hardness and corrosion resistance of the single-layer EP coating and C-EP are analyzed and compared. Furthermore, the corrosion mechanism of C-EP is investigated along with its impact on the magnetic properties of RSM.

2. Experimental

2.1 Preparation of B-RSM and EP Coatings

Figure 1 shows the flowchart of preparation process of B-RSM, E-EP/RSM and C-EP/RSM. The mixed magnetic powder used for the fabrication of this experimental consisted of 74.88 wt.% bonded NdFeB powder (MQP-9-6.5HD, Magnequench (Tianjin) Co., Ltd.), 18.72 wt.% SUS alloy powder (220439B, Haining FeiDa Metallurgy Powder Co., Ltd), 0.15 wt.% lubricant ($C_{36}H_{70}O_4Zn$), 2.5 wt.% binder (W-6C,) and 3.75 wt.% acetone. The fabricated mixed magnetic powder was transferred to the molding machine and pressed under a force of 105 KN. Subsequently, the pressed RSMs were cured in a curing oven at 180 ± 5 °C for 25 mins. After solidification, the sample temperature was allowed to drop to room temperature before beveling and polishing. The RSMs were then washed and dried in an ultrasonic cleaning machine to obtain the final B-RSM.

Following was a description of the preparation process for E-EP/RSM: 470 L of cathodic electrophoretic resin (CR6911/

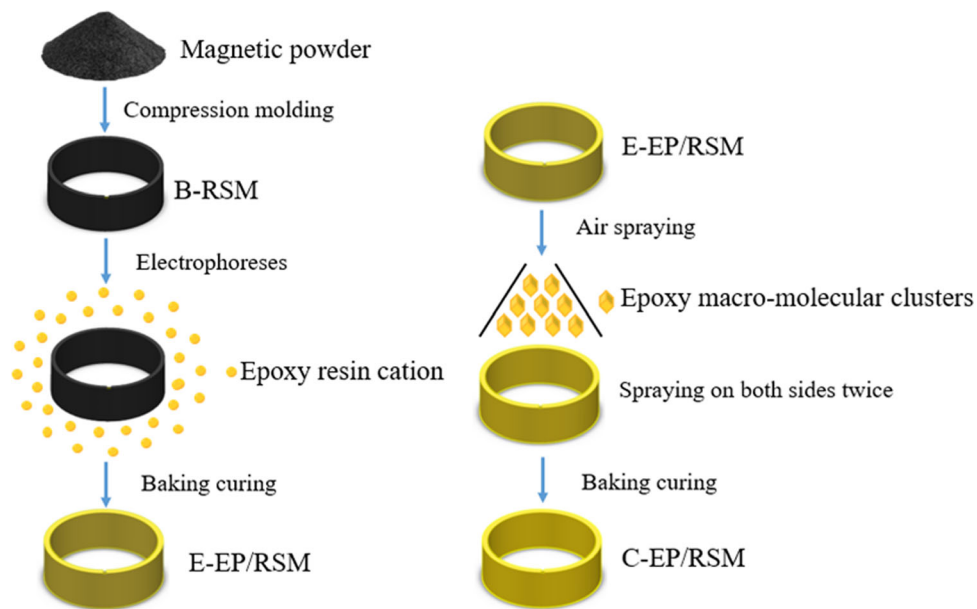


Fig. 1 Preparation process flowchart of B-RSM, E-EP/RSM and C-EP/RSM

200 K-Cl), 10 L of 2-butoxyethanol solvent (PPGSOLVENT-03/16 K-Cl), 70 L of pigment slurry (CP522F/280 K-Cl), and 450 L of pure water were added to the electrophoresis tank in turn. The pigment slurry was composed of 2 epoxy resin, 2-butoxyethanol, dibutyltin oxide, carbon black and water in accordance with 2:2:1:1:4. The electrophoresis circulating pump is turned on to make the electrophoresis tank liquid fully mixed and uniform. An appropriate amount of acetic acid was added to adjust the pH value of the electrophoresis bath to 6, the conductivity of the bath and the anode bath was measured, and kept it at about $2000 \mu\text{S}\cdot\text{cm}^{-1}$. RSMs were immersed in a pure water ultrasonic cleaning tank under the action of the electrophoresis line travel arm for ultrasonic cleaning for 90 s. The cleaned RSMs were passed into the electrophoretic tank with the travel arm, and the electrophoretic voltage was set at 90 V for the electrophoretic coating. The entire electrophoresis lasted for 120 s. After electrophoresis, the E-EP/RSMs were cleaned with solvent in a pure water cleaning tank for 120 s to remove the epoxy paint from the surface of the workpiece. Then, E-EP/RSMs were placed in the vault furnace for baking and curing at a temperature of 180°C for a duration of 20 mins.

The preparation process of C-EP/RSM consisted of two parts. Firstly, a layer of E-EP coating was deposited on the RSM surface by cathodic electrophoresis process. After being cured and cooled to room temperature, E-EP/RSM was placed in an air spraying process and then coated with another EP coating. The EP spray solution consisted of 37.6 wt.% waterborne EP spray paint (HD-EF30) and 62.4 wt.% pure water. The spraying was performed reciprocally using a 0.5-mm-diameter spray gun with a spitting volume of $32\text{--}36 \text{ g}\cdot\text{min}^{-1}$ and an atomization air pressure of 0.3–0.5 Mpa. After spraying twice, the samples were placed in a drying oven and baked at 180°C for 15 mins. The magnets were turned over, and the same treatment was applied to the other side of the samples. After spraying on both sides, the RSMs were cured in an infrared curing oven for 45 mins at 180°C .

2.2 Characterization and Test

The surface and cross-section morphology of B-RSM, E-EP/RSM and C-EP/RSM were characterized by SEM (SU8020, Hitachi), and the composition of EP coating was analyzed by EDS. The surface roughness of samples was measured by AFM (Dimension Icon, Brooke). The porosity of E-EP and C-EP coatings was measured using a N_2 adsorption–desorption apparatus (Autosorb-IQ3, Kantar, USA). The hardness of each sample was measured by microhardness tester (HVS-10Z). The binding force between EP coating and substrate was qualitatively measured by adhesion cross-cut test. The magnetic properties of samples were measured with a permanent magnet material meter. The polarization curves and electrochemical impedance spectra (EIS) of B-RSM, E-EP/RSM and C-EP/RSM in 3.5wt % NaCl solution were measured by electrochemical workstation (Shanghai Chenhua, CHI760E, China). In the experiment, the sample was used as the working electrode (the area was 0.2 cm^2), saturated calomel (SCE) as the reference electrode, and platinum sheet as the counter electrode. All working electrodes were immersed in a 3.5wt. % NaCl solution for 30 mins to achieve a stable electrochemical potential. In the electrochemical test, the test scanning rate was 2 mV/s , the scanning potential was $-1.4 \text{ V}-0 \text{ V}$, the potential amplitude in the EIS measurements was 5 mV , and the

frequency range of EIS is $10^{-3}\text{--}10^6 \text{ Hz}$. The NSS test chamber (AHL-90-CSF, Dongguan Quanyi) was used to create a corrosive environment by continuously spraying 5 wt.% NaCl solution at a temperature of 35°C , while maintaining a saturated barrel temperature of 47°C and pressure of 0.2 MPa. The corrosion status of the specimens was observed and recorded every 24 h.

3. Results and Discussion

3.1 Characterization of Morphology

The morphology of the B-RSM surface is shown in Fig. 2(a). The surface of NdFeB substrate has many cracks and pits of different sizes due to the pressed magnetic powder. The highly uneven surface confirms previous assertions that bonded NdFeB substrates are particularly vulnerable to corrosion due to their inherent structural characteristics. The B-RSM surface exhibits significant fluctuations, with an average surface roughness (S_a) of 178 nm as calculated by NanoScope Analysis 2.0 software (Fig. 2b). In contrast, the E-EP/RSM surface is smooth and flat, and its S_a is the lowest at 26.3 nm (Fig. 2e). After the air spraying process is used to apply another layer of EP onto the E-EP/RSM surface (Fig. 2g), no obvious cracks are observed, but numerous spotted protrusions are present. The surface roughness of C-EP/RSM is primarily determined by the spraying process, and the value of S_a is between the above two, 91.7 nm (Fig. 2h). After comparing AFM images of B-RSM, E-EP/RSM and C-EP/RSM, it is evident that EP coating significantly reduces the surface roughness of RSM due to its excellent film-forming properties. Moreover, it effectively blocks the substrate from corrosive media. From the above data, it can be seen that the EP coating brought by the electrophoresis process has the best leveling characteristics and the least roughness.

Figure 3 shows the SEM cross-sectional morphologies of B-RSM, E-EP/RSM and C-EP/RSM. The RSM substrate was internally spliced by block magnetic powder with a plethora of cracks and holes (Fig. 3a). The coating thickness of E-EP/RSM (Fig. 3b) was measured to be approximately $15 \mu\text{m}$, while that of C-EP/RSM (Fig. 3c) was around $30 \mu\text{m}$. The EP coating formed on the surface of the bonded NdFeB substrate was uniform in thickness, without fluctuations or defects, effectively covered many pores and gaps on the substrate surface. It can also be seen that the tight bonding between the sprayed EP coating on the surface and the electrophoretic EP coating on the bottom is evident, with no discernible boundaries. This can be attributed to both coatings being of the same type of EP, which offers superior material compatibility compared to heterogeneous materials.

The porosity of the coating can directly affect the protective performance of the coating. The BET equation was used to estimate the specific surface area of E-EP and C-EP coatings, and the BJH treatment was applied to the desorption isotherms to calculate the pore size distributions of E-EP and C-EP coatings. It can be seen from Fig. 4 that both coatings are porous structures with pore sizes between 10 and 50 nm. It indicates that the pore distribution of E-EP and C-EP coatings is approximately the same, and the structures are similar. Table 1 summarizes the mean pore diameter, pore volume and BET surface area of the samples. The average pore diameter of

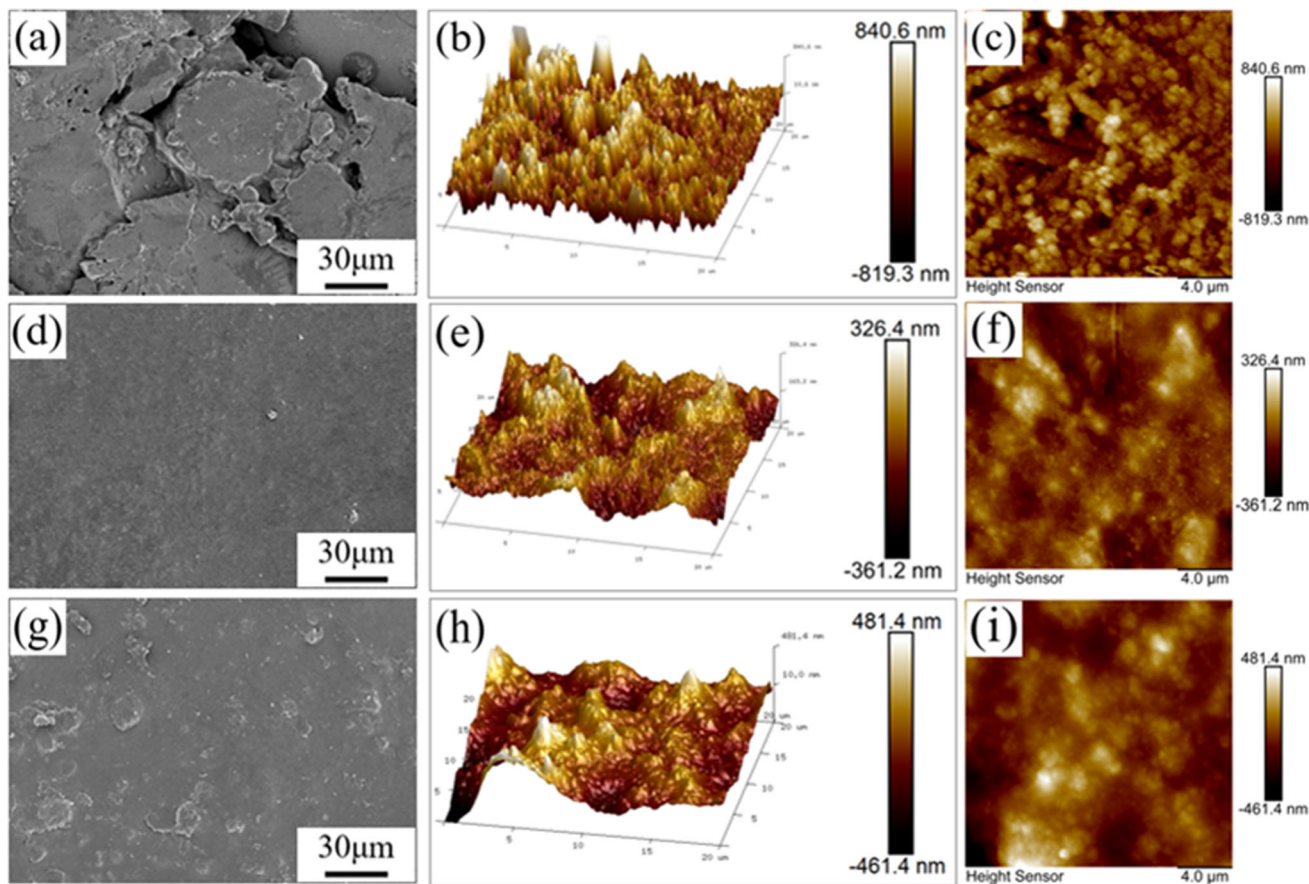


Fig. 2 SEM morphology and AFM images of B-RSM (a), (b), (c), E-EP/RSM (d), (e), (f), C-EP/RSM (g), (h), (i)

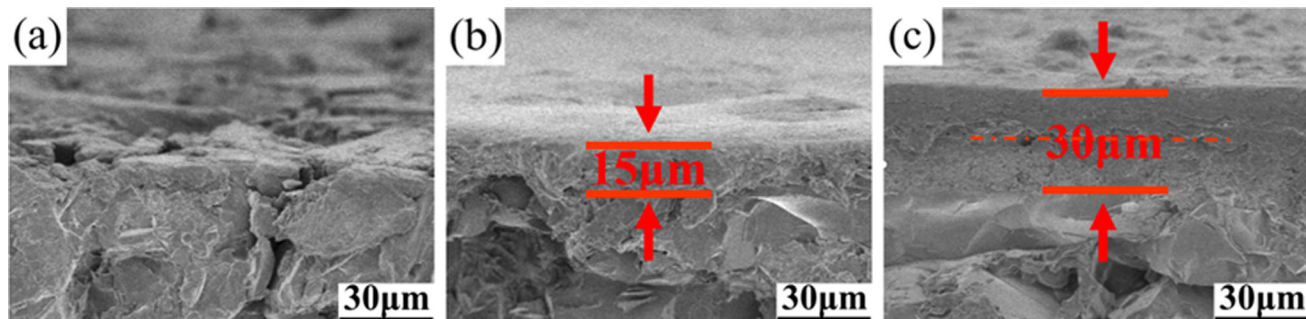


Fig. 3 SEM cross-sectional morphologies: (a) B-RSM; (b) E-EP/RSM; (c) C-EP/RSM

E-EP/BSM is 15.926 nm, which is lower than the average pore diameter of C-EP/BSM at 17.05 nm. The pore volumes of E-EP/BSM and C-EP/BSM are 0.004 cm³/g and 0.003 cm³/g, respectively. The smaller pore volume of C-EP compared to E-RSM also indicates that C-EP has a compact structure and better protective properties.

The distribution of elements on the surface of the samples is illustrated in Fig. 5. It can be observed that Nd and Fe are the main components of B-RSM, while Pr, Ce and Cr peaks indicate doping elements present in the original magnetic powder. Additionally, trace amounts of Mo, La and Ti were also detected. E-EP/RSM and C-EP/RSM exhibit similar compositions. In addition to the organic constituents of C and O, there exist trace amounts of Al and Si elements. As these peaks do not overlap with those of Nd, Fe and B, they will not interfere

with the detection of said elements. The elemental weights in selected areas are presented in Table 2.

As shown in Table 2, B-RSM consists mainly of Nd, Fe, B and C with contents of 4.41, 60.94, 2.65 and 11.84 at.%, respectively. The surface elements of E-EP/RSM and C-EP/RSM are primarily composed of C and O, indicating that the EP coatings exhibit excellent encapsulation effects on RSMs. The combined weight percentages of C and O elements in C-EP/RSM are higher at 90.21 at.%, which shows the stronger sealing characteristics of double-layer EP.

3.2 Analysis of Performance

As can be seen from Fig. 6, after being treated with 3 M tape, the scratch area of the E-EP coating shows no obvious

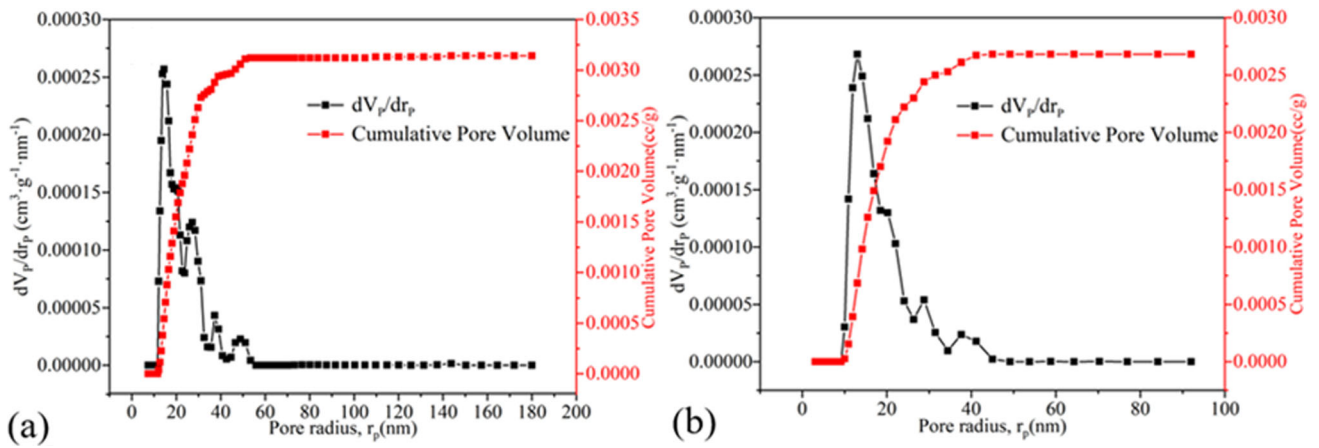


Fig. 4 Pore size distribution curves of N₂ adsorption: E-EP/RSM (a), C-EP/RSM (b)

Table 1 Pore structure parameters of E-EP/RSM and C-EP/RSM

Specimen	BET surface areas, m ² /g	Total pore volume, cm ³ /g	Mean pore size, nm
E-EP/RSM	2.522	0.004	15.629
C-EP/RSM	1.933	0.003	17.050

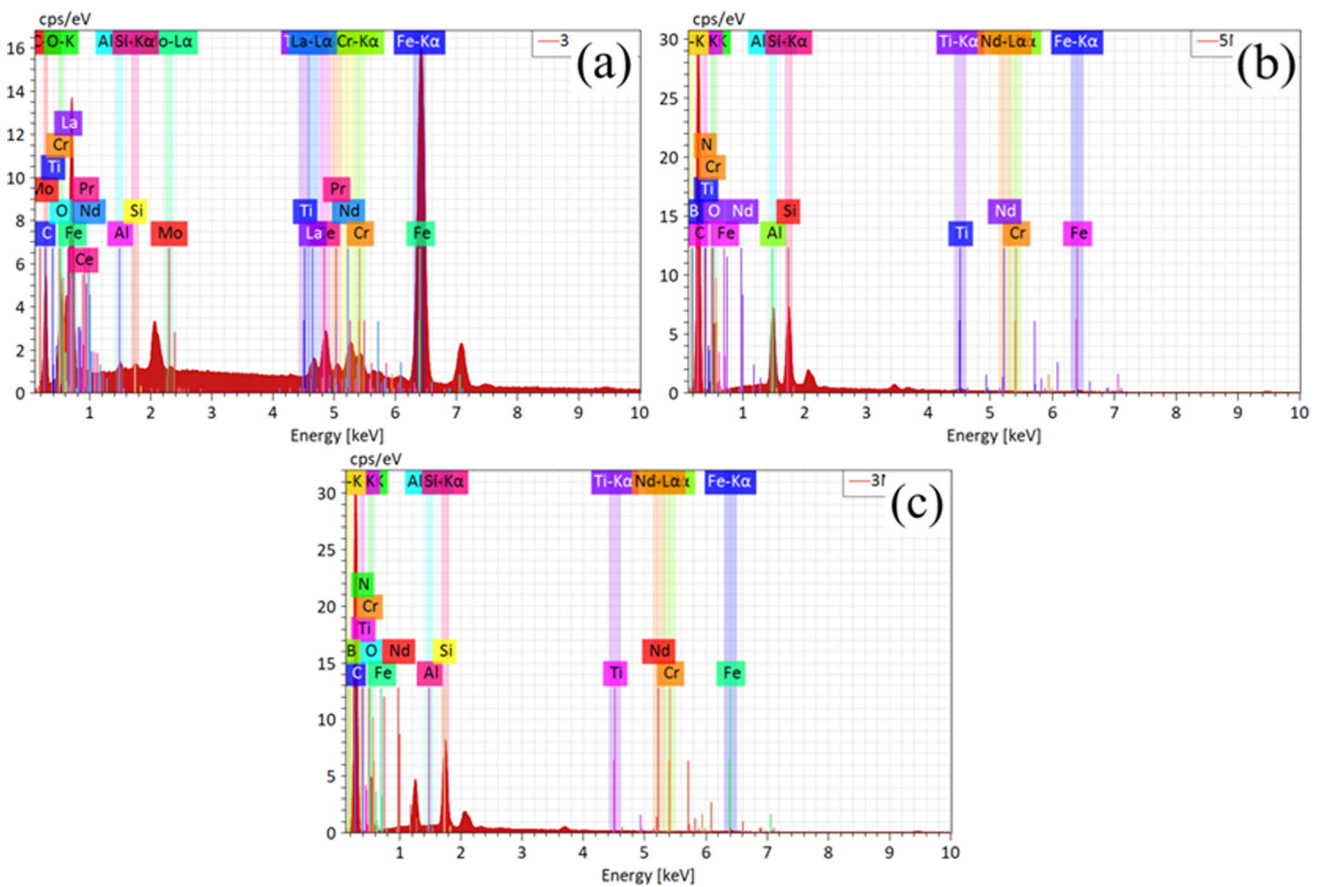
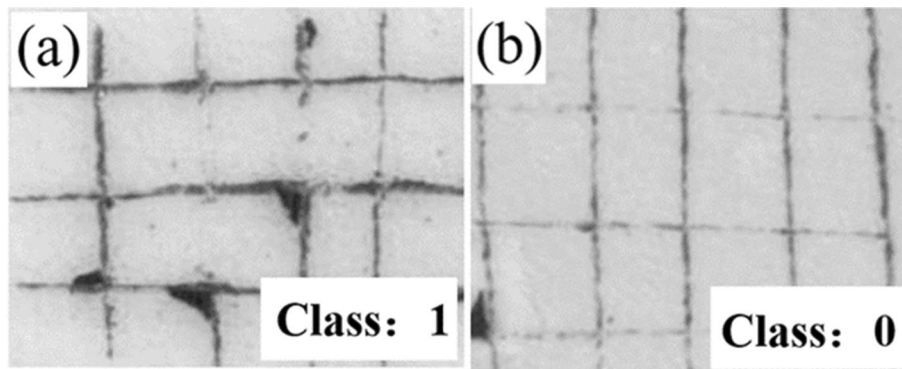
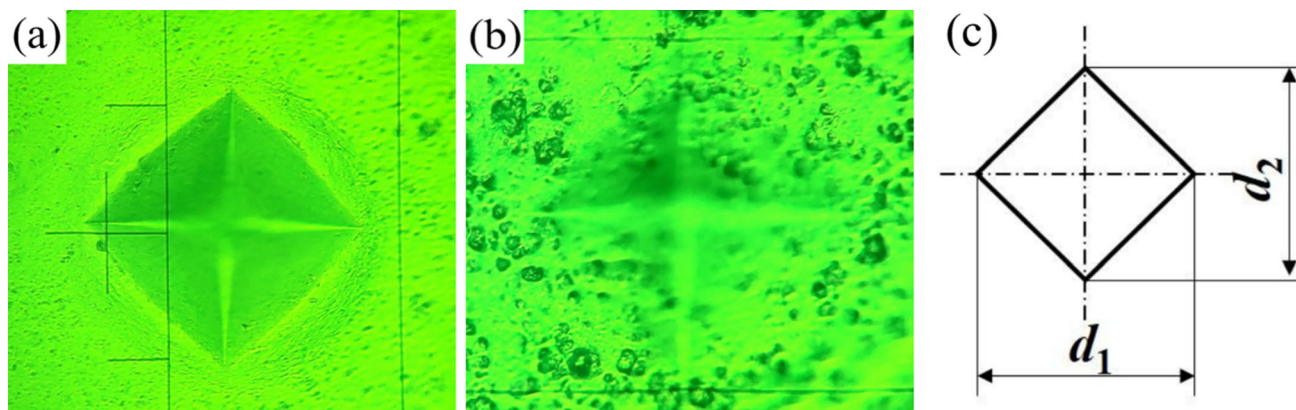


Fig. 5 Analysis of elemental composition on sample surface: (a) B-RSM; (b) E-EP/RSM; (c) C-EP/RSM

Table 2 Weight of sample elements

Sample	Element weight, at. %								
	Nd	Fe	B	C	N	O	Si	Al	Ti
B-RSM	4.41	60.94	2.65	11.84	0.11	4.81	0.21	0.29	0.01
E-EP/RSM	0.01	0.64	3.85	66.43	2.42	19.48	3.60	3.21	0.37
C-EP/RSM	0.01	0.41	3.48	70.89	1.34	19.32	4.54	0.02	0.00

**Fig. 6** Adhesion cross-cut test images of C-EP/RSM (a) and E-EP/RSM (b)**Fig. 7** Microhardness test images of E-EP/RSM (a) and C-EP/RSM (b); The measurement diagram (c)

signs of peeling, and its adhesive level is rated at 0. In contrast, the C-EP coating exhibits some degree of peeling within the scratch area, but less than 5%, resulting in adhesive level rating of 1. The adhesion strength of E-EP coating is a little stronger than that of C-EP. This is due to the fact that the surface roughness of the matrix is correlated with adhesion strength (Ref 17). As substrate surface roughness increases, the real surface area of the substrate surface increases, and the contact area between the coating and the substrate increases, thus increasing the strength of the adhesive force between them. The adhesion strength of C-EP/RSM is influenced by the surface roughness of E-EP/RSM, whereas that of E-EP/RSM is affected by the surface roughness of B-RSM. As the surface roughness of B/RSM is higher than that of E-EP/RSM, the adhesion strength of E-EP coating is correspondingly stronger than that of C-EP coating.

The microhardness of E-EP/RSM and C-EP/RSM is measured using the HVS-10Z digital microhardness tester. The square indentation on the sample test surface is illustrated in Fig. 7. As shown in the figure, the surface of E-EP/RSM appears smoother than that of C-EP/RSM, with a clearer indentation, which is consistent with SEM results. The measurement diagram for the sample is shown in Fig. 7(c). The Vickers hardness value of the sample is calculated according to Eq. 1 by measuring the length of the two diagonal lines d_1 and d_2 of the indentation.

$$Hv = 2F \sin \frac{\alpha}{2} / d^2 \quad (\text{Eq 1})$$

The results show that the average microhardness of E-EP/RSM is 30.977 HV, while the microhardness of C-EP/RSM is 33.623 HV, which is slightly increased compared to that of E-EP/RSM.

As can be seen from the potentiodynamic polarization curves in Fig. 8, compared with B-RSM, the E_{corr} of E-EP/RSM and C-EP/RSM show positive shifts, with values of -0.630 V and -0.412 V, respectively. In corrosive environments, EP itself is not easily reactive with corrosive media and simultaneously acts as a good shielding medium, improving the corrosion resistance of RSM. Compared to E-EP/RSM, the polarization curves of C-EP/RSM exhibit passivation behavior at 10^{-4} and 10^{-5} A/cm². We attribute this to the fact that the double coating additionally increases the limitation of the diffusion of electrolyte ions in the coated film and therefore exhibits passivation at a specific current range. This also indicates that the double-layer EP coating has better corrosion resistance. The polarization curves are analyzed by Tafel extrapolation method, and the corrosion current density (I_{corr}) was extracted, as shown in Table 3. As can be seen from Table 3, the I_{corr} of E-EP/RSM and C-EP/RSM is 4.613×10^{-5} A/cm² and 6.972×10^{-6} A/cm², respectively, which is smaller than the I_{corr} of B-RSM. According to Faraday's law (Ref 18), corrosion rate is proportional to I_{corr} . In the same environment, due to the protective effect of EP coating, the corrosion rate of E-EP/RSM and C-EP/RSM is lower than that of B-RSM, so they have better corrosion resistance. The I_{corr} of C-EP/RSM is the smallest and its corrosion resistance is also the best, so the double-layer EP coating will greatly improve the corrosion resistance of bonded NdFeB magnets.

Figure 9 shows electrochemical impedance spectra (EIS) plots of B-RSM, E-EP/RSM and C-EP/RSM. Figure 9(a), (b), (c) and (d) shows the Nyquist plot, equivalent circuit model,

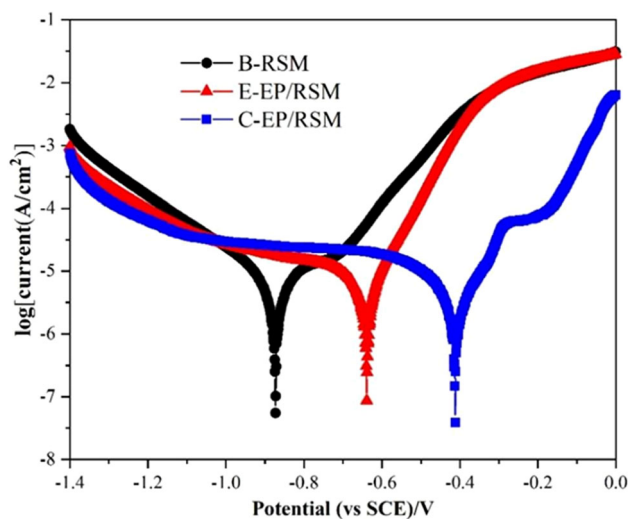


Fig. 8 Potentiodynamic polarization curves of B-RSM, E-EP/RSM and C-EP/RSM

Table 3 Polarization parameters of B-RSM, E-EP/RSM and C-EP/RSM

Specimen	E_{corr} /V	I_{corr} , A/cm ²	Cathodic slope, V/decade	Anodic slope, V/decade
B-RSM	-0.883	6.226×10^{-4}	-0.210	0.209
E-EP/RSM	-0.630	4.613×10^{-5}	-0.151	0.160
C-EP/RSM	-0.412	6.972×10^{-6}	-0.143	0.151

Bode phase angle plot and Bode modulus plot, respectively. It can be seen that a single capacitive resistance arc appeared in all three curves (Fig. 9a). Based on the radius size of the capacitive arc, it can be concluded that C-EP/RSM protective coating exhibits the largest radius, followed by E-EP/RSM and B-RSM in descending order. The magnitude of the capacitive arc's radius is indicative of corrosion rate at matrix-protective layer interface in electrolyte solution. A larger radius corresponds to a slower corrosion rate for the samples. The corrosion rate of the sample can be ranked as C-EP/RSM, E-EP/RSM and B-RSM in ascending order. Therefore, the corrosion resistance follows the same order from high to low.

The equivalent circuit (Ref 19) shown in Fig. 9(b) is used to fit the impedance spectrum in Fig. 9(a). The fitting results of B-RSM, E-EP/RSM and C-EP/RSM impedance parameters are shown in Table 4. R_s and R_{ct} denote the resistance and charge transfer resistance in electrochemical corrosion, respectively. R_{ct} is defined as the value that corresponds to the corrosion resistance when $-Z'' = 0$ corresponds to the value of Z' (Ref 20), and its value corresponds to the diameter of the capacitive arc. CPE, a constant phase angle element, is employed to enhance fitting accuracy by accounting for heterogeneity effects (Ref 21, 22). Compared with E-EP/RSM and B-RSM, C-EP/RSM has the largest R_{ct} value. After 30 min of corrosion, the R_{ct} values of B-RSM, E-EP/RSM and C-EP/RSM are 836.8, 2018 and 2354 $\Omega \cdot \text{cm}^2$. CPE is usually determined by the admittance Y_0 and the dispersion index n (Ref 23). The dispersion index n is between 0.5 and 1, indicating that different degrees of dispersion effect occur on the surface of the magnetic ring. Y_0 reflects the reaction rate of the electrode to a certain extent, and lower Y_0 values indicate a more uniform surface and better corrosion resistance of the coating (Ref 24). C-EP/RSM has the smallest Y_0 and the largest R_{ct} . Therefore, it can be concluded that C-EP/RSM exhibits superior corrosion resistance.

The corrosion inhibition efficiency (IE%) of the coating on B-RSM can be calculated by Eq. 2 (Ref 25), and the results are also given in Table 4:

$$\text{IE}\% = (R_{\text{ct}}^{\text{int}} - R_{\text{ct}}) / R_{\text{ct}}^{\text{int}} \times 100 \quad (\text{Eq 2})$$

where $R_{\text{ct}}^{\text{int}}$ and R_{ct} are the inhibited and uninhibited charge transfer resistance. It can be seen from the table that the IE of E-EP/NdFeB and C-EP/NdFeB were 94.8 and 95.1, which can further prove the above view.

As shown in Fig. 9(c), we can see that the Bode phase angle diagrams of all three samples shows a single peak, indicating that there was only one time constant, which is consistent with that shown by the Nyquist plot. The impedance modulus value is commonly utilized for assessing the corrosion resistance of coating, with higher values in the low-frequency band indicating superior resistance to corrosion (Ref 26). The low-frequency impedance modulus of the samples is C-EP/RSM, E-EP/RSM and B-RSM in descending order (Fig. 9d), and the

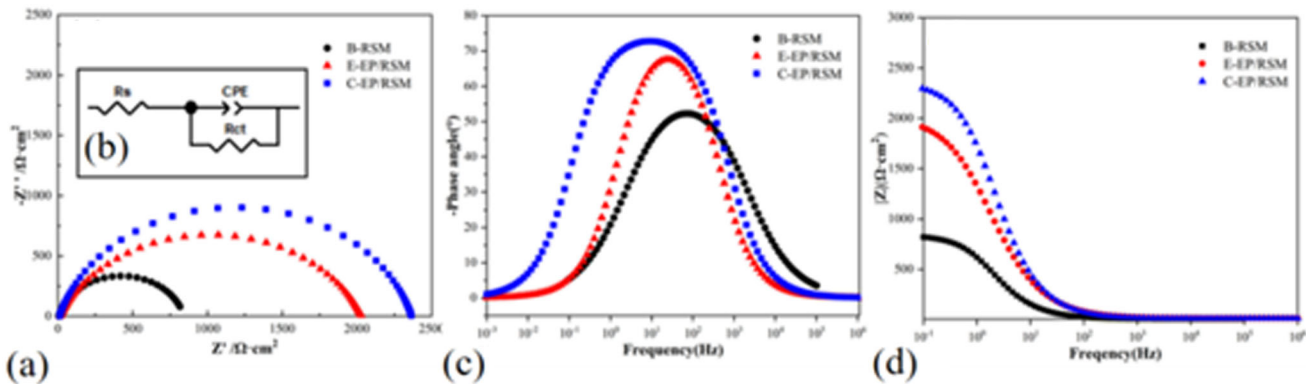


Fig. 9 Nyquist plot (a), equivalent circuit model (b), Bode phase angle plot (c) and Bode modulus plot (d) of B-RSM, E-EP/RSM and C-EP/RSM

Table 4 Impedance parameters of B-RSM, E-EP/RSM and C-EP/RSM

Specimen	$R_e/\Omega, \text{cm}^2$	$R_{ct}/\Omega, \text{cm}^2$	$Y_0/\text{F}\cdot\text{cm}^{-2}\cdot\text{s}^{n-1}$	n	IE., %
B-RSM	6.413	836.8	1.81E-4	0.85707	
E-EP/RSM	13.87	2018	1.05E-4	0.84172	94.8
C-EP/RSM	11.57	2354	6.57E-5	0.83429	95.1

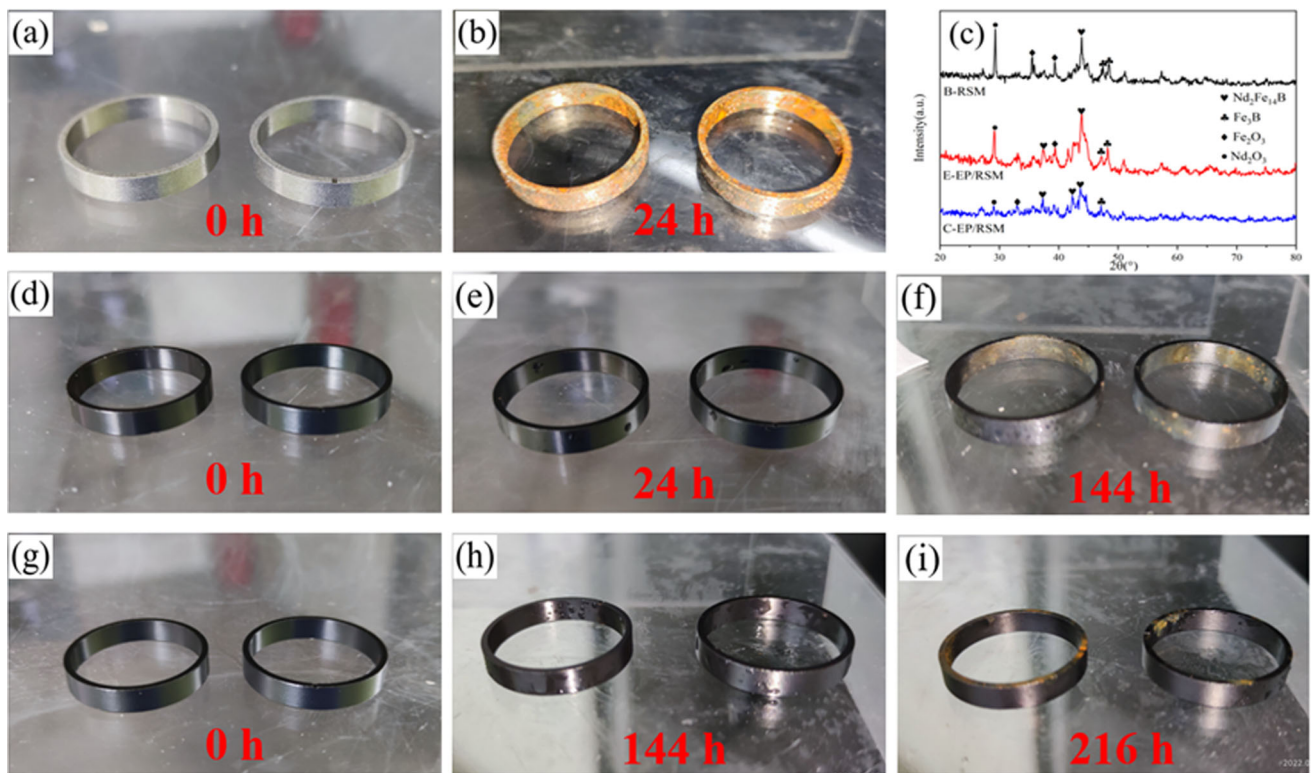


Fig. 10 Surface morphology before and after NSS test: B-RSM (a), (b); E-EP/RSM (d), (e), (f); C-EP/RSM (g), (h), (i) and XRD patterns of B-RSM, E-EP/RSM and C-EP/RSM (c)

impedance modulus decreases gradually with the increase in frequency, so it is also judged by the impedance modulus value that the corrosion resistance of C-EP/RSM is better than E-EP/RSM and B-RSM.

The surface morphologies of NSS tests for B-RSM, E-EP/RSM and C-EP/RSM are shown in Fig. 10. After 24 h of NSS test (Fig. 10b), the surface of B-RSM had a large area of red rust, and the corrosion phenomenon is relatively serious. After

24 h NSS experiment of E-EP/RSM (Fig. 10e), there were no rust spots on the surface. When the NSS time reached 144 h (Fig. 10f), rust appeared on the surface of E-EP/RSM, which was significantly reduced compared with B-RSM, accompanied by local expansion corrosion, and no obvious substrate exposure. On the surface of B-RSM, the EP coating plays a good physical shielding role. After 144 h of contact, the corrosive medium corroded the NdFeB matrix through the corrosion channel of the coating. The corrosion products gradually accumulate and spread to the surface of the coating along the corrosion channel. The optical surface morphology of C-EP/RSM at 144 h of NSS test (Fig. 10h) was basically the same as that before salt spray test, and no obvious rust spots were found on the surface. After 216 h of NSS testing (Fig. 10i), a small amount of red pitting was observed on C-EP/RSM.

The XRD patterns of B-RSM, E-EP/RSM and C-EP/RSM after corrosion (Fig. 10c) are basically the same, with diffraction peaks of the main phase $\text{Nd}_2\text{Fe}_{14}\text{B}$ (JCPDF card: 39-0473), Fe_2O_3 (JCPDF card: 47-1409) and Nd_2O_3 (JCPDF card: 28-0671), which indicates that the EP coatings themselves do not react with the corrosive medium and play the role of physical shielding. These rust spots are mainly Fe_2O_3 and Nd_2O_3 , which are produced by the corrosion of the main phase $\text{Nd}_2\text{Fe}_{14}\text{B}$ and the Nd-rich phase (Ref 27). The NSS time for C-EP/RSM was 1.5 times longer than that of E-EP/RSM. Fewer surface corrosion products were observed on C-EP/RSM, indicating a relatively weak corrosion phenomenon. Therefore, the double-layer EP coatings demonstrated superior corrosion resistance.

The magnetic properties of bonded NdFeB magnets formed by pressing were tested using a permanent magnet material with different temperature B/H curve measuring instrument, so as to detect the influence of coating on the magnetic properties of bonded NdFeB magnets. The demagnetization curves of the coated and uncoated samples are presented in Fig. 11, with extracted magnetic properties listed in Table 5. It can be

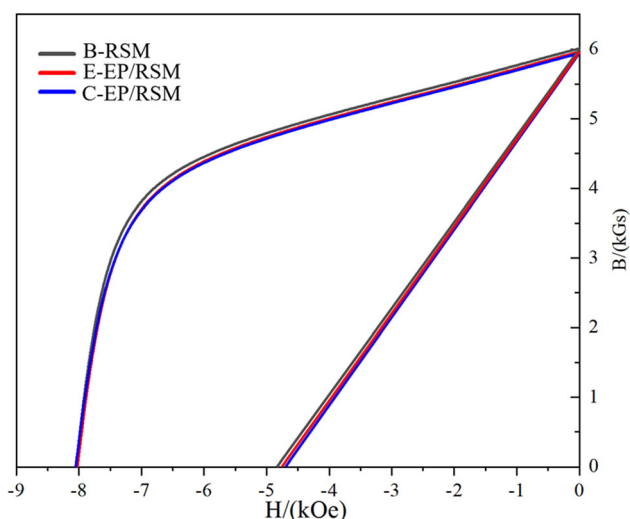


Fig. 11 Demagnetization curves of B-RSM, E-EP/RSM and C-EP/RSM

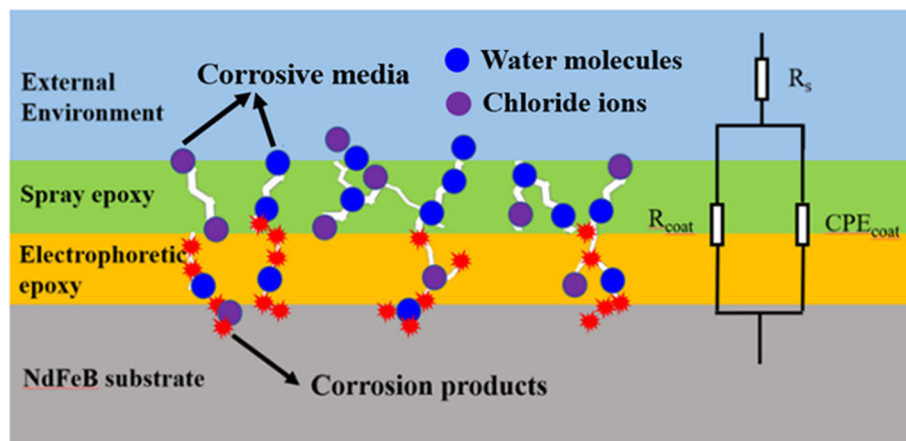
observed that the demagnetization curves of B-RSM, E-EP/RSM and C-EP/RSM almost coincide, indicating that the coating has negligible influence on the magnetic properties of magnets. In comparison with their uncoated counterparts, a slight decrease in remanence (B_r) is observed for the coated samples, with reductions of 0.77% and 1.15% for E-EP/RSM and C-EP/RSM samples, respectively. The endogenous coercivity (H_{cj}) and coercivity (H_{cb}) of the coated samples remain almost unchanged, with a negligible change not exceeding 1.00%. The maximum variation in the $(\text{BH})_{\text{max}}$ of the coating samples is only 2.14%. ZnAl-EP coatings (Ref 28) prepared on bonded NdFeB magnets shows a 7.6% decrease in the maximum magnetic energy product compared to the uncoated samples. In addition, other coating methods such as magnetron sputtered Al coatings (Ref 29), electroplated Al-Mn coatings (Ref 30), and electroless plated Ni-P coatings (Ref 31) have also been found to cause a reduction in magnetic properties (H_{cj} , B_r or $(\text{BH})_{\text{max}}$) of at least 4%. Therefore, the double coatings of C-EP/RSM do not significantly affect the magnetic properties of bonded NdFeB magnets, which is advantageous for their subsequent application and development.

3.3 Corrosion Mechanism

A more detailed analysis of the electrochemical impedance spectrum is conducted based on EIS and the microstructure of bonded NdFeB magnets. An equivalent circuit is utilized to interpret the electrochemical impedance spectrum of C-EP/RSM, as illustrated in Fig. 12. As reported in relevant literature, the microstructure of NdFeB magnets is characterized by porosity (Ref 32, 33). The primary pathway for the diffusion of corrosion electrolyte in NdFeB is through cracks and pores. The coating of the C-EP/RSM consists of a dense inner epoxy layer and a slightly loose outer epoxy layer. Since both epoxy resins are water-soluble epoxy resins, both of them have the same properties, and the two layers are tightly bonded to each other, the two coatings can be regarded as a unified whole. Therefore, the bilayer coating of C-EP/RSM can be considered as a single component R_{coat} . CPE_{coat} and R_{coat} are used to represent the capacitance and resistance of the bilayer coating for fitting and interpreting the EIS of C-EP/RSM. The measured R_{coat} by EIS is associated with the kinetics of anodic dissolution reaction, hence enabling assessment of corrosion resistance in samples based on R_{coat} . The higher the R_{coat} value, the higher the corrosion resistance of the sample. C-EP/RSM exhibits the highest R_{coat} value and thus demonstrates superior corrosion resistance. EIS results obtained are consistent with those from previous kinetic potential polarization curves. Due to its exceptional super-hydrophobicity and corrosion resistance, the double-layer epoxy resin coating effectively prevents corrosive media such as chloride ions and water molecules from penetrating into the substrate. However, it still suffers from fine cracks and holes despite its dense structure. When the NdFeB magnets are exposed to the external corrosive environment, the corrosion factor slowly penetrates and transmits to the junction of the NdFeB matrix and epoxy resin, leading to internal corrosion and generation of corrosion products. The Nd-rich equivalent generated corrosion products are not easily transferred or diffused to external environment, and diffusion channel is blocked, which would lead to the accumulation of corrosion products. It would seriously lead to the bulging and peeling of the coating, and finally lead to the failure of the coating.

Table 5 Magnetic properties of B-RSM, E-EP/RSM and C-EP/RSM

Sample	B_r /kGs	H_{cj} /kOe	H_{cb} /kOe	$(BH)_{max}$ /MGOe
B-RSM	6.008	8.076	4.839	7.288
E-EP/RSM	5.962 (− 0.77%)	8.047 (− 0.36%)	4.805 (− 0.70%)	7.159 (− 1.77%)
C-EP/RSM	5.939 (− 1.15%)	8.026 (− 0.62%)	4.798 (− 0.85%)	7.132 (− 2.14%)

**Fig. 12** Corrosion process diagram of C-EP/RSM

4. Conclusions

In this study, cathodic electrophoretic deposition and air spraying were employed to fabricate a double-layer epoxy resin coating on the bonded NdFeB surface. The findings demonstrated that the EP coating infiltrated into the pores of the NdFeB substrate and exhibited an excellent sealing effect. Another layer of epoxy resin was sprayed on the surface of E-EP/RSM, and the hardness of double-layer EP coatings increased slightly to 33.623 HV. Compared to B-RSM and E-EP/RSM, the I_{corr} of C-EP/RSM decreased by approximately one order of magnitude. Furthermore, the NSS time of C-EP/RSM was 216 h, which was 1.5 times higher than E-EP/RSM, indicating the excellent corrosion resistance of C-EP/RSM. The utilization of identical EP in dual coatings facilitates interlayer adhesion, thereby preventing delamination and promoting coating stability. The synergistic effect of these two layers enhances the anti-corrosion performance of the coating system. Double-layer EP coatings have minimal impact on the magnetic properties of RSM, so it can be widely applied in corrosion resistance research and industrial production of RSM.

Acknowledgments

This study was financially supported by the Fundamental Research Funds for the Central Universities of China (Grant No. PA2022GDGP0029) and the Key Research and Development Program of Anhui Province (202104A05020001).

References

1. M.A. Recai Önal, S. Dewilde, M. Degri, L. Pickering, B. Saje, S. Riaño, A. Walton, and K. Binnemans, Recycling of Bonded NdFeB

- Permanent Magnets using Ionic Liquids, *Green Chem.*, 2020, **22**, p 2821–2830. <https://doi.org/10.1039/D0GC00647E>
2. X.H. Zhang, and W.H. Xiong, Effect of Bonding Process on the Properties of Isotropic Epoxy Resin-Bonded Nd-Fe-B Magnets, *Rare Met.*, 2009, **28**, p 248–252. <https://doi.org/10.1007/s12598-009-0049-8>
3. D.T. Zhang, P.F. Wang, M. Yue, W.Q. Liu, J.X. Zhang, J.A. Sundararajan, and Y. Qiang, High-Temperature Magnetic Properties of Anisotropic MnBi/NdFeB Hybrid Bonded Magnets, *Rare Met.*, 2016 <https://doi.org/10.1007/s12598-015-0668-1>
4. Y. Cao, M. Zhu, M.Z. Rong, and M.Q. Zhang, Injection Moldable, Self-Healable, and Recyclable Rubber-Bonded NdFeB Magnets with the Magnetic Particulates Content up to 90 wt.%, *Adv. Compos. Hybrid. Ma.*, 2023, **6**, p 1–18. <https://doi.org/10.1007/s42114-023-00623-6>
5. M. Lopez, J. Jimenez, and R. Mangalaraja, The Effects of Mechanical Milling on the Structural, Mechanical, and Electromagnetic Properties of Cu-8 wt.% NdFeB Composite Alloys, *J. Compos. Mater.*, 2017, **51**, p 1901–1911. <https://doi.org/10.1177/0021998316664126>
6. F.Q. Zhai, A.Z. Sun, D. Yuan, J. Wang, S. Wu, A.A. Volinsky, and Z.X. Wang, Epoxy Resin Effect on Anisotropic Nd-Fe-B Rubber-Bonded Magnets Performance, *J. Alloy. Compd.*, 2011, **509**, p 687–690. <http://doi.org/10.1016/j.jallcom.2010.09.210>
7. Z. Shi, H. Zeng, Z.J. Zhang, X.W. Zhang, L. Ćurković, V. Mandić, S. Fu, W. Wang, J. Liu, L.Z. Zhao, and X.F. Zhang, Improvement on Corrosion Resistance of Sintered Nd-Fe-B with Bilayer Al/Cr thin Films, *J. Magn. Magn. Mater.*, 2023, **563**, p 170222. <https://doi.org/10.1016/j.jmmm.2022.170222>
8. M.N. Farzam, S. Behrang, M. Ahmadi, and A. Kianvash, Fracture Strength and Surface Magnetic Flux Uniformity in an Isotropic Polymer-Bonded Ring-Shaped Nd-Fe-B Magnet, *J. Mater. Eng. Perform.*, 2018, **27**, p 3972–3977. <https://doi.org/10.1007/s11665-018-3494-4>
9. S. Shi, D.D. Zang, X. Chen, T. Ma, L.H. Gu, D.G. Xu, and J. Liu, Preparation and Properties of a Novel Waterborne Epoxy Resin Modified Emulsified Asphalt, *Constr. Build. Mater.*, 2023, **371**, p 130767. <https://doi.org/10.1016/j.conbuildmat.2023.130767>
10. P.A. Vanessa, U.K. Julieth, G.H. Andres, O.M. Rincon, and G.F. Vargas, Corrosion Protection of Carbon Steel by Alumina-Titania Ceramic Coatings used for Industrial Applications, *Ceram. Int.*, 2018, **44**, p 21765–21773. <https://doi.org/10.1016/j.ceramint.2018.08.273>

11. H. Yan, M. Cai, J.C. Wang, L. Zhang, H. Li, W. Li, X.Q. Fan, and M.H. Zhu, Insight into Anticorrosion/Antiwear Behavior of Inorganic-Organic Multilayer Protection System Composed of Nitriding Layer and Epoxy Coating with $Ti_3C_2T_x$ MXene, *Appl. Surf. Sci.*, 2021, **536**, p 147974. <https://doi.org/10.1016/j.apsusc.2020.147974>
12. Y.H. Dong and Q. Zhou, Relationship Between ion Transport and the Failure Behavior of Epoxy Resin Coatings, *Corros. Sci.*, 2014, **78**, p 22–28. <https://doi.org/10.1016/j.corsci.2013.08.017>
13. J. Chen, J.L. Xu, J. Huang, L. Dai, M.S. Xue, and J.M. Luo, Corrosion Resistance of T-ZnO_n/PDMS-MAO Composite Coating on the Sintered NdFeB Magnet, *J. Magn. Magn. Mater.*, 2021, **534**, p 168049. <https://doi.org/10.1016/j.jmmm.2021.168049>
14. F. Liu, Q. Li, X.K. Yang, Y. Dai, F. Luo, S.Y. Wang, and H.X. Zhang, Corrosion Resistance of Environment-Friendly Sealing Layer for Zn-Coated Sintered NdFeB Magnet, *Mater. Corros.*, 2015, **62**, p 1141–1148. <https://doi.org/10.1002/maco.201006039>
15. H.Y. Wang, S.Y. Zhu, H.Y. Yao, Y.Z. Di, M. Shu, J.H. Li, B. Zhang, G.Z. Cao, and S.W. Guan, Positive Effect of the Addition of Polyaniline on the Anticorrosive Property of Polyethersulfone Two-Layer Composite Coating, *J. Appl. Polym. Sci.*, 2021, **138**, p 50758. <https://doi.org/10.1002/app.50758>
16. Y.W. Yang, L. Yang, Y.Z. Sun, N. Jiang, C.H. Guan, X.G. Fang, and J.G. Liu, Preparation and Corrosion Resistance of Epoxy Resin Coating for Bonded NdFeB Magnet, *Prog. Org. Coat.*, 2022, **173**, p 107180. <https://doi.org/10.1016/j.porgcoat.2022.107180>
17. P.J. Zhang, G.Q. Xu, J.Q. Liu, X.F. Yi, Y.C. Wu, and J.W. Chen, Effect of Pretreating Technologies on the Adhesive Strength and Anticorrosion Property of Zn Coated NdFeB Specimens, *Appl. Surf. Sci.*, 2016, **363**, p 499–506. <https://doi.org/10.1016/j.apsusc.2015.12.073>
18. J.L. Xu, Z.C. Zhong, Z.X. Huang, and J.M. Luo, Corrosion Resistance of the Titania Particles Enhanced Acrylic Resin Composite Coatings on Sintered NdFeB Permanent Magnets, *J. Alloy. Compd.*, 2013, **570**, p 28–33. <https://doi.org/10.1016/j.jallcom.2013.03.033>
19. Y.Y. Cheng, P.X. Pang, K.W. Gao, H.S. Yang, and A.A. Volinsky, Corrosion Resistance and Friction of Sintered NdFeB Coated with Ti/TiN Multilayers, *Thin Solid Films*, 2014, **550**, p 428–434. <https://doi.org/10.1016/j.tsf.2013.10.133>
20. M. Yeganeh, I. Khosravi-Bigdeli, M. Eskandari, and S.R. Alavi Zaree, Corrosion inhibition of L-methionine amino acid as a Green corrosion inhibitor for stainless steel in the H₂SO₄ solution, *J. Mater. Eng. Perform.*, 2020, **29**, p 3983–3994. <https://doi.org/10.1007/s11665-020-04890-y>
21. C. Liu, Q. Bi, A. Leyland, and A. Matthews, An Electrochemical Impedance Spectroscopy Study of the Corrosion Behaviour of PVD Coated Steels in 0.5 N NaCl Aqueous Solution: Part II.: EIS Interpretation of Corrosion Behaviour, *Corros. Sci.*, 2003, **45**(6), p 1257–1273. [https://doi.org/10.1016/S0010-938X\(02\)00214-7](https://doi.org/10.1016/S0010-938X(02)00214-7)
22. H.J. Zhao, L. Liu, Y.T. Wu, and W.B. Hu, Investigation on Wear and Corrosion Behaviour of Cu–Graphite Composites Prepared by Electroforming, *Compos. Sci. Technol.*, 2007, **67**, p 1210–1217. <https://doi.org/10.1016/j.compscitech.2006.05.013>
23. L.J. Wang, M.C. Wang, and H. Chen, Electrochemical Corrosion Behavior of TiAlN/CrN Nanoscale Multilayer Coatings by Multi-Arc Ion Plating in 3.5% NaCl Solution, *Corrosion*, 2020, **76**, p 628–638. <https://doi.org/10.5006/3373>
24. H. Kancharla, G.K. Mandal, H.S. Maharana, S.S. Singh, and K. Mondal, Structure-Dependent Corrosion Behavior of Electrodeposited Zn Coating, *J. Mater. Eng. Perform.*, 2023, **32**, p 2993–3006. <https://doi.org/10.1007/s11665-022-07308-z>
25. M.A. Chidiebere, E.E. Oguzie, L. Liu, Y. Li, and F.H. Wang, Ascorbic Acid as Corrosion Inhibitor for Q235 Mild Steel in Acidic Environments, *J. Ind. Eng. Chem.*, 2015, **272**, p 182–192. <https://doi.org/10.1016/j.jiec.2014.11.029>
26. P.J. Wang, J.X. Cai, X.Q. Cheng, L.W. Ma, Y. Yang, X.J. Xia, and X.G. Li, Fabrication of Chemisorbed Film on Ultrafine-Grained Steels for Corrosion Inhibition in Saline Solution, *Thin Solid Films*, 2023, **766**, p 139657. <https://doi.org/10.1016/j.tsf.2022.139657>
27. X. Li, J. Ni, Z. Wang, B. Song, C. Wang, and X. Cui, Effects of Pressure Holding Time on Magnetic Properties and Corrosion Resistance of Hot-Deformed NdFeB Magnets, *J. Mater. Eng. Perform.*, 2023 <https://doi.org/10.1007/s11665-023-08575-0>
28. Y.W. Yang, N. Jiang, Y.Z. Sun, L. Yang, C.H. Guan, E.H. Zhang, X.G. Fang, and J.G. Liu, Structure and Corrosion Resistance Characteristics of ZnAl/EP Coating on Bonded NdFeB Magnet, *J. Mater. Eng. Perform.*, 2022, **12**, p 5475–5482. <https://doi.org/10.1007/s11665-022-07472-2>
29. J.L. Li, S.D. Mao, K.F. Sun, X.M. Li, and Z.L. Song, AlN/Al Dual Protective Coatings on NdFeB by DC Magnetron Sputtering, *J. Magn. Magn. Mater.*, 2009, **321**, p 3799–3803. <https://doi.org/10.1016/j.jmmm.2009.07.039>
30. J.J. Ding, B.J. Xu, and G.P. Ling, Al–Mn Coating Electrodeposited from Ionic Liquid on NdFeB Magnet with high Hardness and Corrosion Resistance, *Appl. Surf. Sci.*, 2014, **305**, p 309–313. <https://doi.org/10.1016/j.apsusc.2014.03.067>
31. Z. Chen, A. Ng, J.Z. Yi, and X.F. Chen, Multi-Layered Electroless Ni-P coatings on Powder-Sintered Nd-Fe-B Permanent Magnet, *J. Magn. Magn. Mater.*, 2005, **302**, p 216–222. <https://doi.org/10.1016/j.jmmm.2005.09.008>
32. J.L. Xu, Z.X. Huang, J.M. Luo, and Z.C. Zhong, Corrosion Behavior of Sintered NdFeB Magnets in Different Acidic Solutions, *Rare Metal Mater. Eng.*, 2015, **44**, p 786–790. [https://doi.org/10.1016/S1875-5372\(15\)30047-3](https://doi.org/10.1016/S1875-5372(15)30047-3)
33. J.L. Xu, Q.F. Xiao, D.D. Mei, Y.X. Tong, Y.F. Zheng, L. Li, and Z.C. Zhong, Microstructure, Corrosion Resistance and Formation Mechanism of Alumina Microarc Oxidation Coatings on Sintered NdFeB Permanent Magnets, *Surf. Coat. Technol.*, 2017, **309**, p 621–627. <https://doi.org/10.1016/j.surfcoat.2016.12.023>

Publisher's Note Springer Nature remains neutral with regard to jurisdictional claims in published maps and institutional affiliations.

Springer Nature or its licensor (e.g. a society or other partner) holds exclusive rights to this article under a publishing agreement with the author(s) or other rightsholder(s); author self-archiving of the accepted manuscript version of this article is solely governed by the terms of such publishing agreement and applicable law.